

# Long: Programmable Droplets: Leveraging digitally-responsive flow fields to actively tune liquid morphologies

## Short: Active flow fields for programmable liquid morphologies

**Authors:** Raphael Kay<sup>1\*</sup>, Charlie W. Katrycz<sup>2</sup>, Ethan J. Heimlich<sup>3</sup>, Benjamin D. Hatton<sup>2</sup>

### **Affiliations:**

<sup>1</sup>Department of Mechanical and Industrial Engineering, University of Toronto; Toronto, Canada.

<sup>2</sup>Department of Materials Science and Engineering, University of Toronto; Toronto, Canada.

<sup>3</sup>Department of Statistical Sciences, University of Toronto; Toronto, Canada.

\*Corresponding author: raphael.kay@mail.utoronto.ca

### **Abstract**

Stimulus-responsive materials enable programmable and adaptive behaviors. Typical solid-phase systems can only achieve small deformations for applications where shape transformations are beneficial or required. Liquids, in contrast, can self-assemble and achieve very high strains in a multilayered environment. Here we report liquid droplet formation by tuning flow potential within a confined fluidic cell. We digitally inject small volumes of liquid-pigment into an otherwise-transparent liquid layer, generating macroscopic droplet assembly over large areas constrained between closely-spaced plates. Droplet morphology is actively controlled by modulating outlet conditions to tune flow fields. Pattern stability is maintained through control over injection rate, interfacial viscosity difference, and interfacial surface tension. We demonstrate time-dependent droplet formation and migration to achieve spatially-tunable optical properties. Applied as a multi-cell array, we imagine this liquid mechanism will enable scalable pattern dynamics for active shading and visual display technologies.

**Keywords:** *self-assembly, active fluidics, smart materials, liquid shading*

### **Introduction**

Smart materials, which are typically characterized by an integrated capacity to sense, control, and actuate in response to an applied stimulus, enable trainable and reactive behaviors at the material scale (1-3). Conventionally, solid-phase systems achieve volumetric changes and/or shape deformations, caused by microscopic changes of the lattice structure, when subjected to thermal (4, 5), optical (6, 7), hygroscopic (8-12), or electric stimuli (13, 14). In this article, we instead propose a liquid-phase smart material system that achieves pigment self-assembly under the influence of tunable potential liquid flow. We manipulate various boundary pressures within

a confined fluidic cell, enabling flow-responsive liquid deformation in a reversible and repeatable manner.

Intermolecular forces are much weaker in liquids than solids. As a result, liquids easily flow and can be simply manipulated. Pressure-induced liquid flow has been leveraged to achieved dynamic thermal (15-19) and optical (15) properties in materials. Infrared-absorbing liquids, for instance, can be pumped through a window-embedded vasculature, enabling cooling effects along the building interface (15). Liquids stored within a deformable bladder can also be displaced to proportionally measure pressure, providing a microfluidic mechanism for active sensing and display (20). Moreover, fluids can carry nano- and microscopic particles that enable more sophisticated responses to applied stimuli. For example, colloidal suspensions of ferro- or ferrimagnetic particles can form complex ferrofluidic morphologies in applied magnetic fields (21-24).

Capillary interactions, which occur at the length-scale of a fluidic droplet, can also dictate sophisticated and choreographed liquid movements. Droplets can be manipulated on solid surfaces by topographical (25-27), chemical (25, 28, 29), or electrical (30, 31) patterning. Through designed functional gradients, liquids can be made to overcome resistant forces, enabling directed droplet transport in a specified direction. One famous study demonstrated how a gradient in surface free energy (hydrophobicity) could cause a water droplet to run uphill (27).

Liquid morphologies can also be controlled within confined multifluid environments. In particular, fluid dynamics are commonly investigated in Hele-Shaw cells – comprising a thin liquid layer constrained between two closely-spaced rigid plates. Viscosity-driven interfacial instabilities, for instance, are widely characterized within Hele-Shaw systems, where a less viscous fluid is introduced into a more viscous fluid under pressure (32). Known as the Saffman-Taylor (viscous fingering) instability, liquid patterns emerge due to small perturbations in their flow. These perturbations can propagate along the multifluid interface, forming fractal-like branching features (33-35).

In this work, we present a new mechanism for tuning liquid droplet morphology: programmable potential flow. We demonstrate control over droplet shape and position by switching the pressure condition (i.e., either open to atmosphere or closed) of a series of active valves along a Hele-Shaw cell boundary. This control over pressure allows us to manipulate local flow fields, enabling time-dependent droplet shape-change and migration. By tuning the interfacial properties between droplet and host liquid phases, we ensure stable interfacial growth. And by introducing precise concentrations of pigment particles within these liquid droplets, we can use

flow fields to tune patterns of optical transmission and absorption across a cell. This liquid smart material can be demonstrated from the microscopic to macroscopic length-scale. And we speculate that this generalizable methodology for switchable droplet morphology and migration will enable new possibilities for dynamic display, communication, camouflage, and shading.

## Materials and Methods

We fabricated a modified Hele-Shaw cell, constrained by two rigid PMMA plates (30x30x0.6 cm<sup>3</sup>). Plates were separated and sealed at the edges using a 2-mm-thick double-sided elastomer adhesive (3M). We machined one central injection port at the center of, and eight outlet ports around the boundary of, one of the two PMMA plates (Fig. 1a). We connected the central inlet using tubing to a bi-directional, NE-1010 digital syringe pump, and we connected switchable valves to each of the eight outlet ports. We opened all boundary valves, and filled the Hele-Shaw cell with a clear castor oil (891 cP).

To generate a pigment-phase droplet, we introduced an aqueous suspension of carbon black (891 cP) into the castor oil already present within the Hele-Shaw cell. Carbon particles were sonicated to decrease particle clustering and improve suspension longevity. The pigment phase represented a suspension of carbon black at a concentration of 0.2 g/50 mL of a glycerol-water mixture (note that glycerol and water are miscible in all proportions, and can mix with no significant change in relative molar volumes (36)). The viscosity of the glycerol-water mixture was calculated using the four-parameter correlation of temperature-dependence on aqueous glycerol solution viscosities, presented by Chen and Pearlstein (37). Calculated values were then compared to those generated experimentally by Segur and Oberstar (38). We tested the viscosity effect of the carbon black by comparing timed capillary flow through a Cannon-Fenske capillary viscometer for both a sample of distilled water and a distilled water suspension of carbon, and confirmed a negligible difference (< 1%). The viscosity of the castor oil phase was also calculated experimentally using a Cannon-Fenske capillary viscometer, and interfacial surface tension between the pigment and oil phases was estimated from the literature (36). Finally, optical spectra for both the pigment and oil phase liquids, were measured with a PerkinElmer Lambda 1050 Spectrometer (three-detector module).

Droplets were introduced within Hele-Shaw cell (25 mL/min), displacing the host castor oil towards the boundary outlets. Outlet valves were switched for each potential flow configuration, and open valves were connected to drainage tubing, collecting in a shared reservoir open to the atmosphere. Droplets were then reversibly collapsed by reversing the flow on the syringe pump.

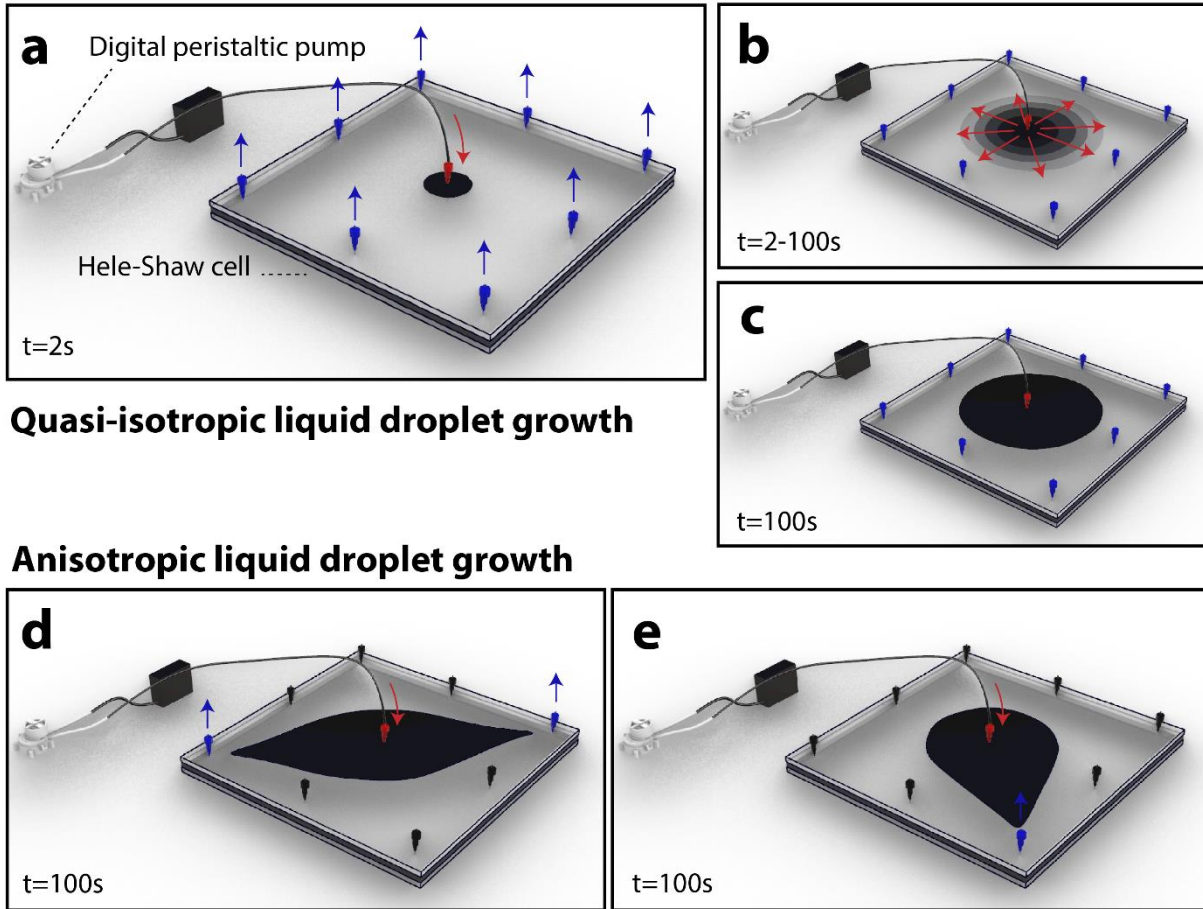
Static, steady-state, potential flow, for each outlet configuration, was approximated by calculating an electric potential field (MATLAB code adapted from (39)), mathematically analogous to the hydrodynamic potential within a Hele-Shaw cell. We assumed Darcy Flow within a constant field, where instantaneous flow rate is proportional to the pressure gradient,  $q \propto \nabla P$ , analogous to an electromotive model where field strength is proportional to the gradient of electrostatic potential,  $E \propto \nabla I$ .

## Results

### Reversible Quasi-isotropic Droplet Injection

We injected viscous, aqueous phase, pigments into a transparent oil phase contained within a Hele-Shaw cell. Each of the eight outlet boundaries of the cell was opened to atmospheric pressure (Fig. 2a), and pigment was injected at a rate of 25 mL/min. Pigment droplets grew radially under a quasi-isotropic potential field (Fig. 2a-c, Fig. 3a). Consistent with a perfect circle, droplet area increased with the square of its radius (Fig. 3b), and droplet perimeter increased linearly with its radius (Fig. 3c).

Droplet growth was reversible (Fig. 3a), and pattern collapse was also consistent with a circular morphology (Fig. 3b-c). Reversibility was aided by a semi-elastic Hele-Shaw cell design. PMMA plates exhibited slight bowing during droplet expansion, where plate deformation increased closer to the central inlet. This elastic capacity, coupled with a high interfacial surface tension between the aqueous and oil liquid phases ( $\sigma=32.5$  dyn/cm), enabled complete droplet growth reversibility, achievable across several pigment expansion and retraction cycles ( $n > 50$ ).



### Quasi-isotropic liquid droplet growth

### Anisotropic liquid droplet growth

**Figure 1. Working principle of active droplet formation.** (a-c) Digitally-driven quasi-isotropic pigment injection within Hele-Shaw fluid cell. (d-e) Anisotropic droplet formation over time achieved through dynamic control of flow field.

### Stable Interfacial Growth

Critical in the control of global droplet morphology is the management of interfacial stability. The pigment droplet interface is susceptible to unstable branching phenomena when introduced at high velocities to displace host liquids within Hele-Shaw cells (32). Within a vertical Hele-Shaw cell, unstable finger growth along the droplet interface occurs when the amplification factor,  $a > 0$ , for:

$$(1) \quad a = \frac{2\pi}{\lambda} \left\{ \frac{12V}{b^2} (n_1 - n_2) + g(\rho_1 - \rho_2) \right\} - \frac{8\pi^3 \sigma}{\lambda^3}$$

Where  $n_1$  is the host fluid viscosity,  $n_2$  is the invading guest fluid viscosity,  $\rho_1$  is the host density,  $\rho_2$  is the guest density,  $g$  is the gravitational constant,  $V$  is the interfacial velocity,  $b$  is the gap height between plates,  $\sigma$  is the interfacial surface tension, and  $\lambda$  is the wavelength (finger width) of the instability (32). For non-branching, stable growth, we can set the instability wavelength to the maximum circumference of the droplet, thereby avoiding unstable fingering. From Equation (1), by setting the aqueous pigment and oil phase viscosities even, and by performing droplet injection in the horizontal plane, perpendicular to gravity, we obtain a new expression for the amplification factor:

$$(2) \quad a = \frac{-8\pi^3\sigma}{\lambda^3}, \text{ for } n_1 - n_2 = 0 \text{ and } g = 0.$$

Critically, we see that for necessarily positive values of  $\sigma$  and  $\lambda$ , the amplification factor will always be negative so long as  $n_1 - n_2 = 0$  and  $g = 0$ . Viscosity-matching therefore underlies interfacial stability for droplet growth within a horizontal Hele-Shaw cell. As such, a glycerol-water solution (891 cP) is injected into a castor oil (891 cP) of the same viscosity across all experimental sequences ( $n_1 - n_2 = 0$ ).

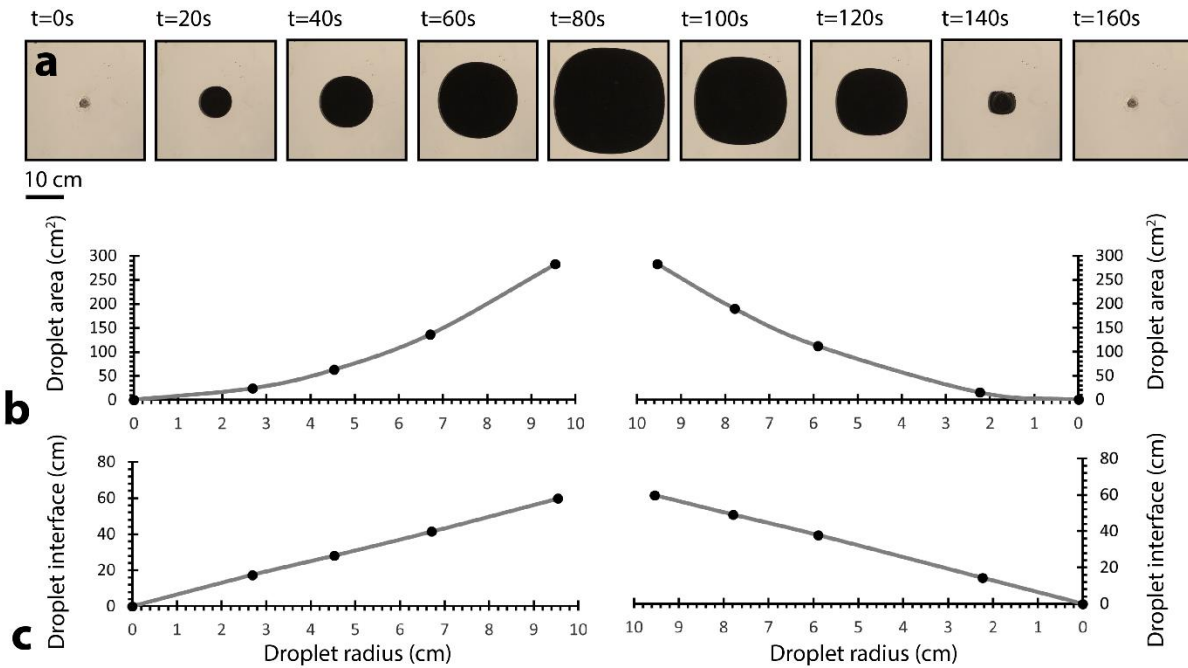


**Figure 2.** (a) Reversible pigment droplet dispersal and retraction under quasi-isotropic flow field. (b) Droplet area as a function of droplet radius, where droplet area is proportional to

dispersed volume, for reversible droplet dispersal and retraction sequence. (c) Droplet interface (perimeter) as a function of droplet radius for reversible droplet dispersal and retraction sequence.

### **Anisotropic Droplet Injection**

We again injected viscous, aqueous phase, pigments into a transparent oil phase contained within a Hele-Shaw cell. This time, however, outlet valves along the cell boundary were selectively closed (Fig. 3a), generating anisotropic potential flow across the cell (estimated in Fig. 3b). Pigment was injected at a rate of 25 mL/min, and droplets grew under an anisotropic field (Fig. 3c). Droplets developed initially with a radial morphology (Fig. 3c, Fig. 4a-d), where anisotropic potential flow was not sufficient to overcome droplet surface energy and host fluid viscosity. After 30 seconds (12.5 mL of pigment injected), however, pigment droplets began to deform according to the potential flow gradient estimated in Fig. 3b (Fig. 3d, Fig. 4a-d).

At equilibrium, pigment droplets expanding within a confined Hele-Shaw cell will assume a circular shape, to minimize surface energy. Under a hydrodynamic flow field, however, viscous stresses (proportional to the flow shear rate, and viscosity) will act on the droplet to cause it to deform. Accordingly, there is a competition between forces acting on the droplet: the viscous forces to deform, and the capillary forces (through surface tension) acting to return the droplet to an equilibrium shape.

The approximate morphology of the droplet deformation can more specifically be explained by a toy model for electrostatic potential. Mathematically, in an electrostatic model, field strength is proportional to the gradient of electrostatic potential,  $E \propto \nabla I$ . In our analogous hydrodynamic model, which broadly explains the emergence of droplet morphology by assuming Darcy Flow, instantaneous flow rate is proportional to the pressure gradient,  $q \propto \nabla P$ . We can interchange these simple models because both  $I$  (current) and  $P$  (pressure) in respective systems go as the inverse of the distance from a point charge or outlet ( $\propto 1/r$ ). In total, we injected 20 mL of pigment into the Hele-Shaw cell, and observed continuous, accelerated droplet deformation according to this hydrodynamic gradient (Fig. 3b) – even after the culmination of pigment injection (Fig. 3c, Fig. 4a-d). Droplets deformed, as if attracted, to open outlets. This was expected from our toy model, where pressure increases closer to an outlet.

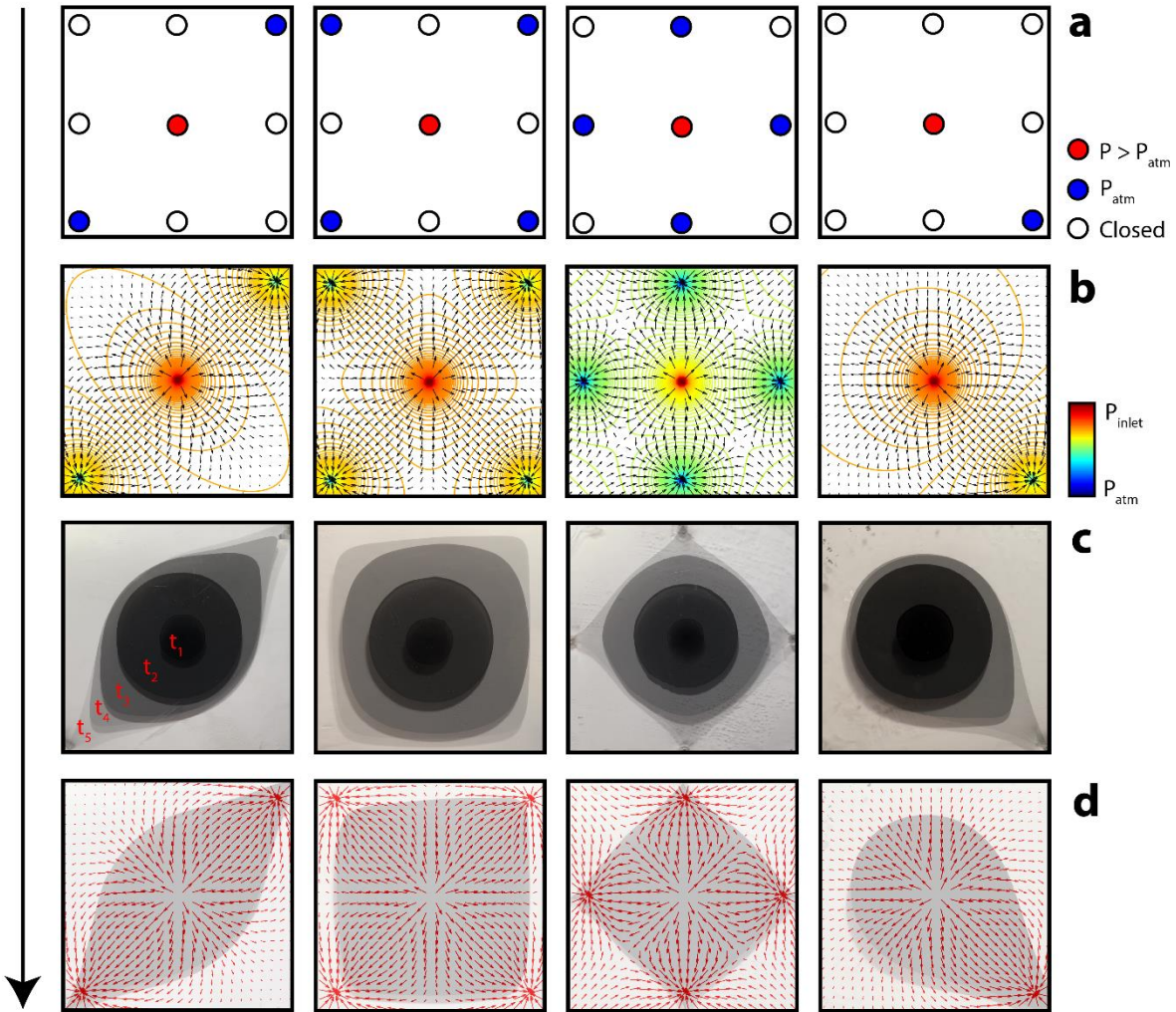


**Figure 3. Pigment dispersal across variable anisotropic flow fields.** (a) Four Hele-Shaw cell states with spatially-varied outlet boundary conditions. (b) Estimated (idealized) potential flow field from cell configurations in a. (c) Overlaid time-series images demonstrating anisotropic droplet growth over time. (d) Final droplet configuration from c with overlaid gradient vector field from b.

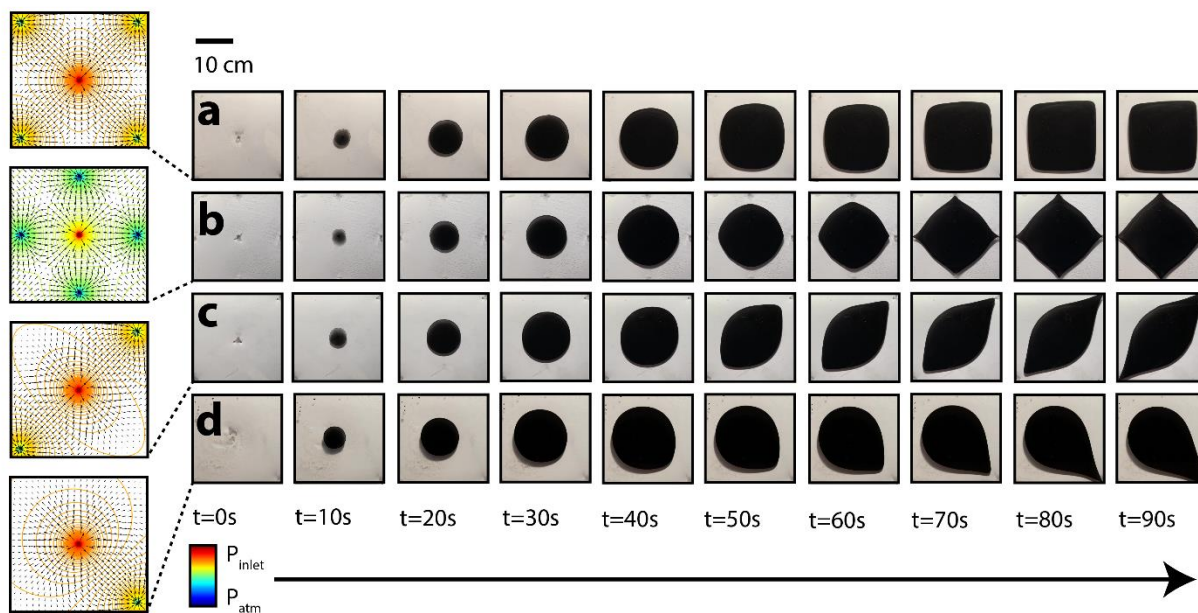


**Figure 4.** Time-dependent droplet growth under four unique potential flow fields (a-d).

### Time-dependent Droplet Morphology Characterization

Droplet morphology changed with time under anisotropic flow fields (Fig. 4a-d). Active injection in all cases lasted approximately 48 seconds (20 mL, at 25 mL/min), while deformation continued until the active droplet reached a boundary outlet (approximately 100 seconds). We first characterized droplet growth and deformation over time for both single-outlet (Fig. 5a) and double-outlet (Fig. 5b) cell configurations (Fig. 4d and Fig. 4c, respectively). The left graphs in Fig. 5 describe droplet deformation as a function of time. Droplet deformation, defined here as the change in droplet length in the direction of greatest possible deformation (i.e., towards an outlet) moves linearly with time. The right graphs in Fig. 5 describe area-normalized droplet deformation as a function of pigment coverage. Normalized droplet deformation, defined here as the relative difference between the droplet length in the direction of greatest potential and the droplet length in the direction perpendicular to the direction of greatest potential, increases later in the growth process, and rapidly ( $> 30\%$ , right graphs, Fig. 5). In the single-outlet case, we see that relative droplet deformation almost exclusively occurs after the injection sequence has finished, as the full 50% relative deformation is achieved with only a 6% change in pigment area coverage (40%-46%) (Fig. 5a, right graph). In the double-outlet case, relative droplet deformation occurs exclusively in the final half of pigment injection (between 25-49% area coverage) (Fig. 5b, right graph). In both these injection sequences, accelerated flow along the droplet tip closest to the outlet was observed, consistent with expected flow outcome from the estimated gradient fields

(Fig. 3b).

For injection sequences corresponding to quad-outlet configurations (Fig. 4a-b), we characterized time-dependent pigment morphology as droplets grew from circles to approach the shape of a square (Fig. 6a-b, respectively). For a corner-diagonal distribution of boundary outlets (outlet at each corner), droplets changed in morphology from the theoretical minimum area difference from the best fit circle (0%, as the droplets were near-circles) to approach the theoretical maximum area difference from the best fit circle (28%, as the droplets became squares) (Fig. 6a). As flow potential was distributed across all corners of the cell, and outlets were positioned at a maximum distance from the central injection site ( $d = \sqrt{2}r$ ), where  $r$  is half a boundary length of the square cell, the fixed-volume (20 mL) pigment droplet did not reach any of the four outlet boundaries. Accordingly, a near-square morphology was reached prior to complete injection (Fig. 6a, decreasing slope between 55-59% area coverage).

For an edge-midpoint distribution of boundary outlets (outlet at each edge midpoint), droplet deformation also increased from the theoretical minimum area difference from the best fit circle (0%) to approach the theoretical maximum area difference from the best fit circle (28%, square) (Fig. 6b). While flow potential was again across multiple regions of the cell, outlets were positioned at a distance 29% closer ( $\{\sqrt{2}r - r\}/\sqrt{2}r$ ) from the central injection site ( $d = r$ ), enabling the pigment droplet to reach outlet boundaries. Accordingly, unlike the injection sequence demonstrated in Fig. 6a, the rate of pigment deformation increased continuously across the entire injection sequence (Fig. 6b, increasing slope).

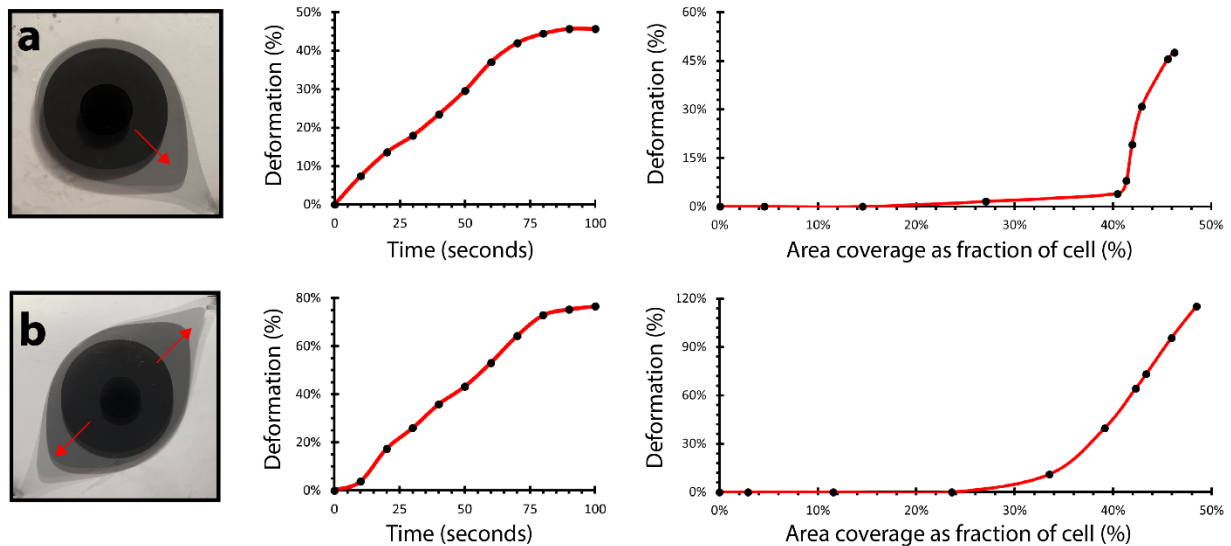


**Figure 5.** Non-normalized (a) single-outlet and (b) multioutlet droplet deformation as a function of time (left graphs) and area-normalized droplet deformation as a function of fractional area coverage, proportional to dispersed pigment volume (flow rate = 25 mL/min).

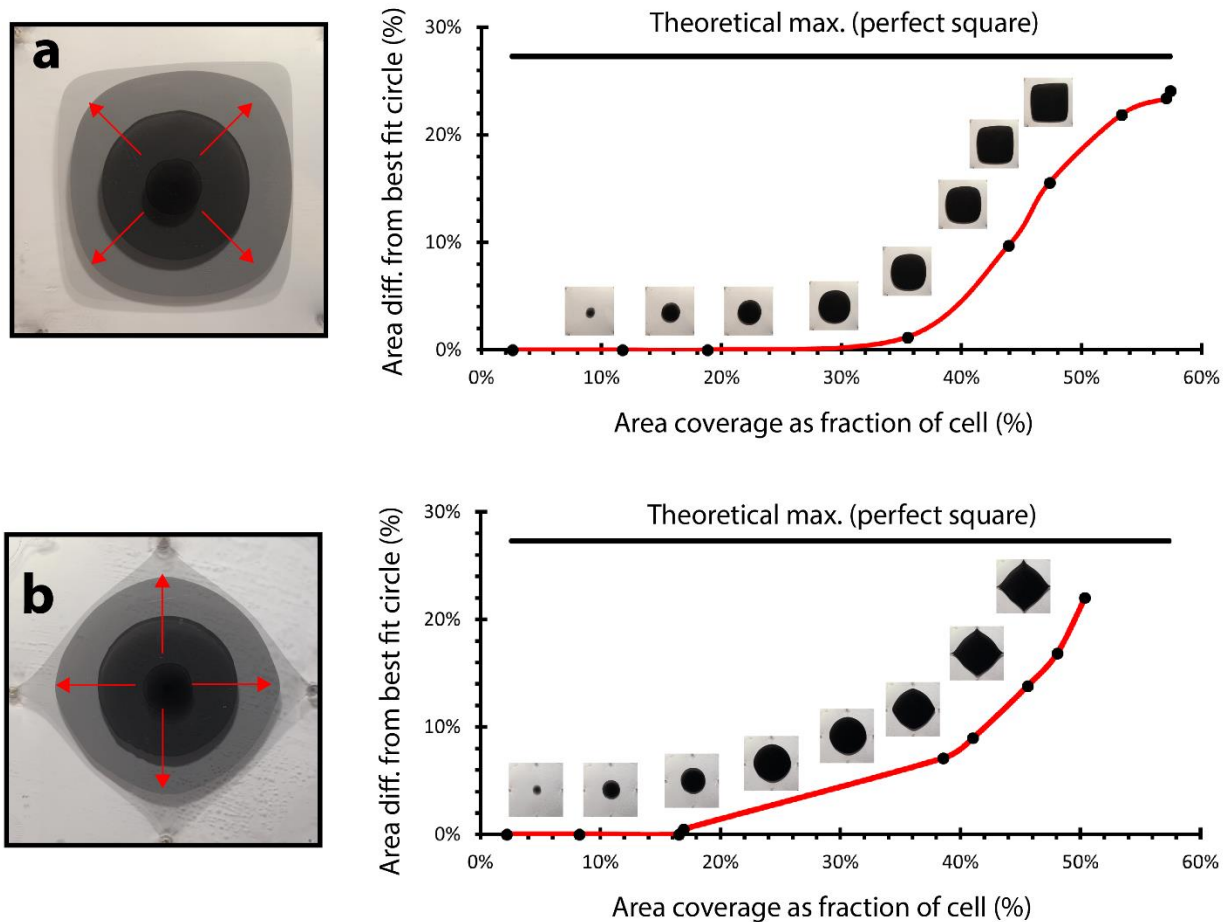


**Figure 6.** Circular droplets become more square-like over time. Quad-outlet droplet deformation as a function of fractional area coverage, proportional to dispersed pigment volume (flow rate = 25 mL/min), for both (a) corner outlet configuration and (b) edge midpoint outlet configuration.

### Time-dependent Droplet Migration

Beyond droplet morphology tunability, we also demonstrated the capacity for complete droplet migration. More than just controlling shape, the capability to choreograph the movement of a droplet, and, in aggregate, a sequence of droplets, might enable more versatile and efficient display systems. Far less material and energy are required to move a pigment droplet across a

cell than to orchestrate several sequential droplet growth and retraction sequences that can only simulate droplet movements in low resolution. We fabricated a multiport Hele-Shaw cell, with two injection ports situated at opposite cell regions (Fig. 7), and a series of evenly-distributed outlet drains (open to atmospheric pressure) to enable drainage proportional to injected pigment volume. We injected two pigment droplets simultaneously into the cell, and let the fluid within the cell reach a pressure-equilibrium. We then closed all outlet drains, and retracted one of the two pigment droplets completely. Through this retraction sequence, we generated a pressure-driven flow field from the injection port with the remaining droplet to the injection port with the recently-retracted droplet. Over 90 minutes, we observed complete droplet migration, until the fluid cell once again reached a pressure-equilibrium (Fig. 7,  $t=1-90$  min).

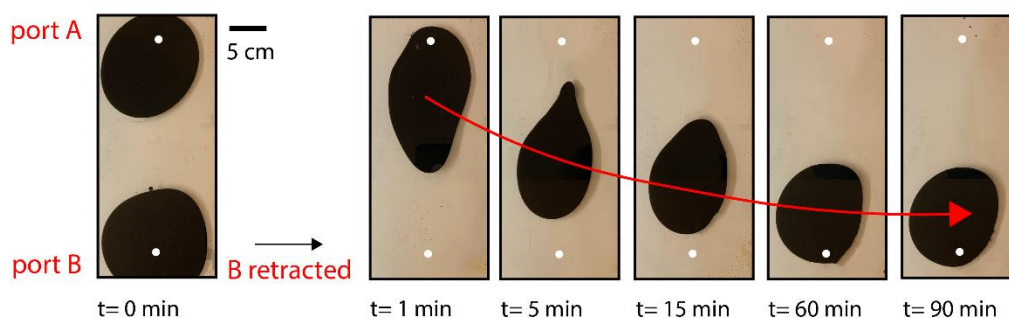


**Figure 7.** Multiport time-dependent droplet migration due to a hydrodynamic potential.

### **Multiport Patterning**

We fabricated a multicell display, designed as a 2x2 array of the Hele-Shaw system illustrated in Fig. 1. We demonstrated differential pattern dynamics within the array, generating independent, digitally-switchable responses across each Hele-Shaw cell (Fig. 8a). We imagine the upscaling of this array, and generated digital multicell pattern arrangements to visualize more complex, coordinated pigment droplet responses (Fig. 8b). To emphasize the potential of this system as a large-area adaptive display, we developed a computational program to read binary digital images and map, based on localized greyscale values, appropriate experimental pattern results: larger pigment droplets were proportionally mapped to darker greyscale pixel values (Fig. 8c-d). We extrapolated time-dependent pattern emergence (Fig. 8c) to achieve course-resolution grey-scale imagery (e.g., an Albert Einstein portrait; Fig. 8d).

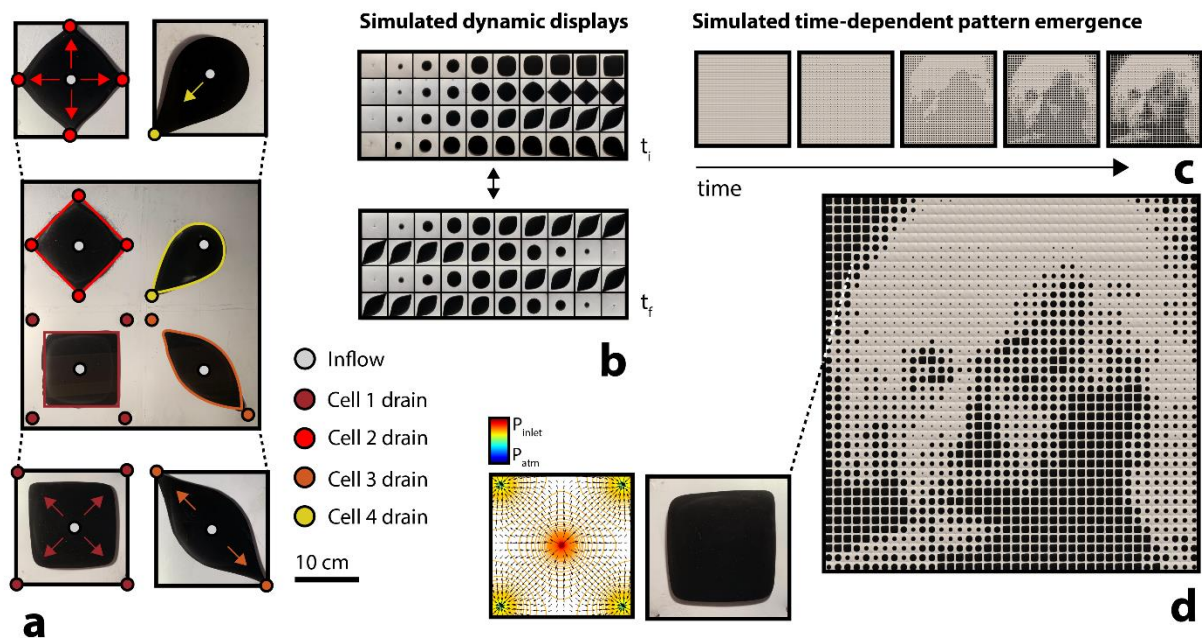


**Figure 8. Fabricated and simulated multipixel visual displays.** (a) Image of a built quad-cell display, where each array element demonstrates a unique flow field and pigment droplet morphology ( $t=100$  s after injection). (b) Examples of switchable digitally-generated multicell displays (unbuilt). (c) Simulated pattern emergence to achieve a predefined multicell visual array (d). Static flow field displayed next to corresponding pigment cell.

## Discussion

### Differential Optical Programmability

We have demonstrated a methodology for generating dynamic pigment morphologies within confined fluidic cells. Active droplet growth and migration enables spatially-tunable optical properties, where precise optical absorption and transmission can be programmed both locally, by actively controlling flow potential and growth, and globally, by scaling pixelated fluid control across large-area arrays. We characterized optical transmission in both the visible and near-infrared spectrum for the transparent host phase (castor oil), and the aqueous pigment phase (glycerol carbon suspension) for an optical path-length of 3 mm within our cell (Fig. 9). We generated active spatiotemporal switching between host and pigment liquid phase optical properties, which can induce changes to both visible light transmittance and solar heat gain (Fig. 9). We also demonstrated significant differences in optical transmission within the visible spectrum for a range of aqueous-phase carbon suspension concentrations (Fig. 9). Fluids have

easily-tunable absorption properties (40, 41), and fluid flow represents a novel and scalable mechanism for large-area optical control.

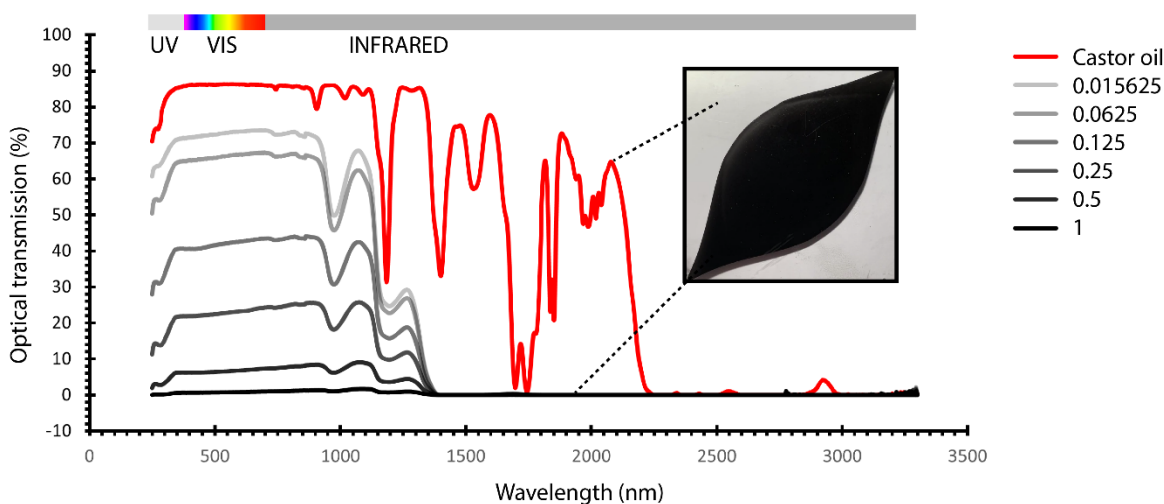


**Figure 9.** Differential visible and near-infrared light transmission between the aqueous pigment phase (grey curves) and oil phase (red curve) for a 3 mm optical path length. Grey curves represent varied concentrations of aqueous carbon black suspensions, where values describe concentration in g of C per 50 mL of H<sub>2</sub>O.

### Reversibility Limitations

Large fluid deformations introduce reversibility constraints. High-viscosity, high-surface-tension liquids decrease undesired fluid mixing (droplet ‘island’ formation), however, above an estimated capillary length (~20 cm), pigment droplets are still susceptible to splitting (separation of droplets) during retraction. Additionally, droplet growth becomes irreversible once the pigment interface extends into an outlet boundary. With this constraint, Hele-Shaw cell length-scale also dictates the maximum pigment droplet size. In our work, within a 30x30x0.2 cm<sup>3</sup> Hele-Shaw cell, we report reversible droplet morphology for droplets up to 22 cm in length (73% the length of the cell).

### Future Work

We have introduced and demonstrated a simple material mechanism for transforming the shape of a two-dimensional pigment droplet within a confined cell. We speculate that the development of multicell arrays, coupled with centralized digital control over valve switching and pigment injection, will enable more sophisticated morphological outputs, for light regulation and surface

display applications. We propose increasing the resolution of valve control by increasing the density of outlets (i.e., the density of control), not only along cell edges, but within the cell region. Additional characterization is required to understand the time-dependent flow and hydrodynamic potential that underlies droplet migration. We propose the development of a larger multiport Hele-Shaw cell, within which more sophisticated droplet movements, fusions, and separations, can be digitally-choreographed and performed. Ultimately, the work described here demonstrates a proof-of-concept. More advanced mechanical techniques concerned with integrating pigment and drain storage, as well as electronic valve, driver, and pump equipment, are required to achieve continuous, reversible, high-resolution pigment display.

### **Data availability**

All data can be made available by the authors upon reasonable request.

### **Acknowledgements**

#### **Funding**

Canadian Foundation for Innovation (CFI) #31799 (BDH)

Percy Edward Hart Professorship, University of Toronto (BDH)

#### **Author contributions**

Conceptualization: RK, CWK

Methodology: RK, CWK, BDH

Experimentation: RK

Visualization: RK

Simulation: EJH

Funding acquisition: BDH

Writing – original draft: RK

Writing – review and editing: RK, CWK, EJH, BDH

### **References**

1. Cao W, Cudney HH, Waser R. Smart materials and structures. *Proceedings of the National Academy of Sciences*. 1999;96(15):8330.
2. Schwartz M. *Smart materials*: CRC press; 2008.
3. Addington M. Contingent Behaviours. *Architectural Design*. 2009;79(3):12-7.
4. Formentini M, Lenci S. An innovative building envelope (kinetic façade) with Shape Memory Alloys used as actuators and sensors. *Automation in Construction*. 2018;85:220-31.
5. Tolley MT, Felton SM, Miyashita S, Aukes D, Rus D, Wood RJ. Self-folding origami: shape

memory composites activated by uniform heating. *Smart Materials and Structures*. 2014;23(9):094006.

6. Liu Z, Liao J, He L, Gui Q, Yuan Y, Zhang H. Preparation, photo-induced deformation behavior and application of hydrogen-bonded crosslinked liquid crystalline elastomers based on  $\alpha$ -cyanostilbene. *Polymer Chemistry*. 2020;11(37):6047-55.

7. Liu Y, Boyles JK, Genzer J, Dickey MD. Self-folding of polymer sheets using local light absorption. *Soft Matter*. 2012;8(6):1764-9.

8. Correa D, Papadopoulou A, Guberan C, Jhaveri N, Reichert S, Menges A, et al. 3D-Printed Wood: Programming Hygroscopic Material Transformations. *3D Printing and Additive Manufacturing*. 2015;2(3):106-16.

9. Tibbits S. 4D Printing: Multi-Material Shape Change. *Architectural Design*. 2014;84(1):116-21.

10. Raviv D, Zhao W, McKnelly C, Papadopoulou A, Kadambi A, Shi B, et al. Active Printed Materials for Complex Self-Evolving Deformations. *Scientific Reports*. 2014;4(1):7422.

11. Kay R, Nitiema K, Correa D. The Bio-inspired Design of a Self-propelling Robot Driven by Changes in Humidity. In: Werner L, Koering D, editors. *Proceedings of the 38th eCAADe Conference; September 16-18, 2020; Berlin, Germany 2020*. p. 233-42.

12. Menges A, Reichert S. Material Capacity: Embedded Responsiveness. *Architectural Design*. 2012;82(2):52-9.

13. Xu C, Stiubianu GT, Gorodetsky AA. Adaptive infrared-reflecting systems inspired by cephalopods. *Science*. 2018;359(6383):1495.

14. Rossiter J, Yap B, Conn A. Biomimetic chromatophores for camouflage and soft active surfaces. *Bioinspir Biomim*. 2012;7(3):036009.

15. Hatton BD, Wheeldon I, Hancock MJ, Kolle M, Aizenberg J, Ingber DE. An artificial vasculature for adaptive thermal control of windows. *Solar Energy Materials and Solar Cells*. 2013;117:429-36.

16. Katrycz CW, Hatton BD. Bioinspired Microfluidic Cooling. In: Deng T, editor. *Bioinspired Engineering of Thermal Materials*. Weinheim, Germany: Wiley-VHC; 2018.

17. Ismail KAR, Henríquez JR. Thermally effective windows with moving phase change material curtains. *Applied Thermal Engineering*. 2001;21(18):1909-23.

18. Chow T-T, Li C. Liquid-filled solar glazing design for buoyant water-flow. *Building and Environment*. 2013;60:45-55.

19. Chow T-T, Li C, Lin Z. Thermal characteristics of water-flow double-pane window. *International Journal of Thermal Sciences*. 2011;50(2):140-8.

20. Mor H, Yu T, Nakagaki K, Miller BH, Jia Y, Ishii H. Venous Materials: Towards Interactive Fluidic Mechanisms. *Proceedings of the 2020 CHI Conference on Human Factors in Computing*

Systems; Honolulu, HI, USA: Association for Computing Machinery; 2020. p. 1–14.

21. Neuringer JL, Rosensweig RE. Ferrohydrodynamics. *The Physics of Fluids*. 1964;7(12):1927-37.
22. Rosensweig RE, Zahn M, Shumovich R. Labyrinthine instability in magnetic and dielectric fluids. *Journal of Magnetism and Magnetic Materials*. 1983;39(1):127-32.
23. Oliveira RM, Miranda JA. Fully nonlinear simulations of ferrofluid patterns in a radial magnetic field. *Physical Review Fluids*. 2020;5(12):124003.
24. Seibold Z, Grinham J, Geletina O, Ahanotu O, Sayegh A, Weaver J, et al. Fluid equilibrium: Material computation in ferrofluidic castings. 2018.
25. Bjelobrk N, Girard H-L, Bengaluru Subramanyam S, Kwon H-M, Quéré D, Varanasi KK. Thermocapillary motion on lubricant-impregnated surfaces. *Physical Review Fluids*. 2016;1(6):063902.
26. Chen H, Zhang P, Zhang L, Liu H, Jiang Y, Zhang D, et al. Continuous directional water transport on the peristome surface of *Nepenthes alata*. *Nature*. 2016;532(7597):85-9.
27. Chaudhury MK, Whitesides GM. How to Make Water Run Uphill. *Science*. 1992;256(5063):1539.
28. Ichimura K, Oh S-K, Nakagawa M. Light-Driven Motion of Liquids on a Photoresponsive Surface. *Science*. 2000;288(5471):1624.
29. Daniel S, Chaudhury MK, Chen JC. Fast Drop Movements Resulting from the Phase Change on a Gradient Surface. *Science*. 2001;291(5504):633.
30. Sun Q, Wang D, Li Y, Zhang J, Ye S, Cui J, et al. Surface charge printing for programmed droplet transport. *Nature Materials*. 2019;18(9):936-41.
31. McHale G, Brown CV, Newton MI, Wells GG, Sampara N. Dielectrowetting Driven Spreading of Droplets. *Physical Review Letters*. 2011;107(18):186101.
32. Saffman PG, Sir Geoffrey Taylor FRS. The penetration of a fluid into a porous medium or Hele-Shaw cell containing a more viscous liquid. In: Pelcé P, editor. *Dynamics of Curved Fronts*. San Diego: Academic Press; 1958. p. 155-74.
33. Bischofberger I, Ramachandran R, Nagel SR. Fingering versus stability in the limit of zero interfacial tension. *Nature Communications*. 2014;5(1):5265.
34. Bischofberger I, Nagel SR. Fluid instabilities that mimic animal growth. *Physics Today*. 2016;69:70-1.
35. Bischofberger I, Ramachandran R, Nagel SR. An island of stability in a sea of fingers: emergent global features of the viscous-flow instability. *Soft Matter*. 2015;11(37):7428-32.
36. Takamura K, Fischer H, Morrow NR. Physical properties of aqueous glycerol solutions. *Journal of Petroleum Science and Engineering*. 2012;98-99:50-60.
37. Chen YM, Pearlstein AJ. Viscosity-temperature correlation for glycerol-water solutions.

Industrial & Engineering Chemistry Research. 1987;26(8):1670-2.

38. Segur JB, Oberstar HE. Viscosity of Glycerol and Its Aqueous Solutions. Industrial & Engineering Chemistry. 1951;43(9):2117-20.

39. Donadio L. Electric Potential and Electric Field. <https://github.com/lorenzolds/partitions/issues/2> 2016.

40. Reilly S, Arasteh D, Rubin M. The effects of infrared absorbing gasses on window heat transfer: A comparison of theory and experiment. Solar Energy Materials. 1990;20(4):277-88.

41. Stopper J, Böing F, Gstoehl D, editors. Fluid Glass Façade Elements: Influences of dyeable Liquids within the Fluid Glass Façade 2013.